

Evaluating European ECOSTRESS Hub Evapotranspiration Products Retrieved from Three Structurally Contrasting SEB Models over Europe

Tian Hu¹, Kaniska Mallick², Patrik Hitzelberger¹, Yoanne Didry¹, Gilles Boulet³, Zoltan Szantoi⁴, Benjamin Koetz⁴, Itziar Alonso⁴, Madeleine Pascolini-Campbell⁵, Gregory H Halverson⁶, Kerry Cawse-Nicholson⁶, Glynn Hulley⁶, Simon J. Hook⁷, Nishan Bhattarai⁸, Albert Olioso⁹, Jean-Louis Roujean¹⁰, Philippe Gamet¹⁰, and Z. Bob Su¹¹

¹Luxembourg Institute of Science and Technology

²LIST

³CESBIO/IRD, France

⁴European Space Agency

⁵NASA Jet Propulsion Laboratory

⁶Jet Propulsion Laboratory, California Institute of Technology

⁷California Institute of Technology

⁸University of Oklahoma

⁹UMR EMMAH - INRAE

¹⁰CESBIO

¹¹Faculty of Geo-Information Science and Earth Observation, University of Twente

December 7, 2022

Abstract

The ECOSystem Spaceborne Thermal Radiometer Experiment on Space Station (ECOSTRESS) is a scientific mission that collects high spatio-temporal resolution (~ 70 m, 1-5 days average revisit time) thermal images since its launch on 29 June 2018. As a predecessor of future missions, one of the main objectives of ECOSTRESS is to retrieve and understand the spatio-temporal variations in terrestrial evapotranspiration (ET) and its responses to soil water availability. In the European ECOSTRESS Hub (EEH), by taking advantage of land surface temperature retrievals, we generated ECOSTRESS ET products over Europe and Africa using three structurally contrasting models, namely Surface Energy Balance System (SEBS) and Two Source Energy Balance (TSEB) parametric models, as well as the non-parametric Surface Temperature Initiated Closure (STIC) model. A comprehensive evaluation of the EEH ET products was conducted with respect to flux measurements from 19 eddy covariance sites over 6 different biomes with diverse aridity levels. Results revealed comparable performances of STIC and SEBS (RMSE of ~ 70 W m⁻²). However, the relatively complex TSEB model produced a higher RMSE of ~ 90 W m⁻². Comparison between STIC ET estimate and the operational ECOSTRESS ET product from NASA PT-JPL model showed a difference in RMSE between the two ET products around 50 W m⁻². Substantial overestimation (>80 W m⁻²) was noted in PT-JPL ET estimates over shrublands and savannas presumably due to the weak constraint of LST in the model. Overall, the EEH is promising to serve as a support to the Land Surface Temperature Monitoring (LSTM) mission.

Evaluating European ECOSTRESS Hub Evapotranspiration Products Retrieved from Three Structurally Contrasting SEB Models over Europe

Tian Hu¹, Kaniska Mallick^{1,10}, Patrik Hitzelberger², Yoanne Didry², Gilles Boulet³, Zoltan Szantoi^{4,8}, Benjamin Koetz⁴, Itziar Alonso⁴, Madeleine Pascolini-Campbell⁵, Gregory Halverson⁵, Kerry Cawse-Nicholson⁵, Glynn C. Hulley⁵, Simon Hook⁵, Nishan Bhattarai⁶, Albert Olioso⁷, Jean-Louis Roujean³, Philippe Gamet³, Bob Su⁹

¹Department of Environment Research and Innovation, Luxembourg Institute of Science and Technology, Belvaux 4362, Luxembourg, ²Department of IT for Innovative Services, Luxembourg Institute of Science and Technology, Belvaux 4362, Luxembourg, ³Centre d'Etudes Spatiales de la Biosphère, CNES, CNRS, INRAE, IRD, UPS, Toulouse 31401, France, ⁴Science, Applications & Climate Department, European Space Agency, Frascati 00044, Italy, ⁵Jet Propulsion Laboratory, California Institute of Technology, Pasadena, California 91109, USA, ⁶Department of Geography and Environmental Sustainability, University of Oklahoma, Norman, Oklahoma 73019, USA, ⁷Unité de Recherche écologie des Forêts Méditerranéennes, INRAE, Avignon, France, ⁸Stellenbosch University, Stellenbosch 7602, South Africa, ⁹Department of Water Resources, Faculty of Geo-Information Science and Earth Observation (ITC), University of Twente, P.O. Box 217, Enschede, 7500 AE, The Netherlands, ¹⁰Department of Environmental Science, Policy and Management, University of California, Berkeley, California 94720, USA

Corresponding author: Tian Hu (tian.hu@list.lu), Kaniska Mallick (kaniska.mallick@list.lu)

Key Points:

- Evaporation products over Europe and Africa were generated using 3 different models (STIC, SEBS, and TSEB) in the European ECOSTRESS Hub
- Comparison at 19 eddy covariance sites revealed noteworthy model divergence with increasing aridity and vegetation sparseness
- A substantial overestimation of the official NASA ECOSTRESS ET product was found under high water limitations

Abstract

The ECOSystem Spaceborne Thermal Radiometer Experiment on Space Station (ECOSTRESS) is a scientific mission that collects high spatio-temporal resolution (~ 70 m, 1-5 days average revisit time) thermal images since its launch on 29 June 2018. As a predecessor of future missions, one of the main objectives of ECOSTRESS is to retrieve and understand the spatio-temporal variations in terrestrial evapotranspiration (ET) and its responses to soil water availability. In the European ECOSTRESS Hub (EEH), by taking advantage of land surface temperature retrievals, we generated ECOSTRESS ET products over Europe and Africa using three structurally contrasting models, namely Surface Energy Balance System (SEBS) and Two Source Energy Balance (TSEB) parametric models, as well as the non-parametric Surface Temperature Initiated Closure (STIC) model. A comprehensive evaluation of the EEH ET products was conducted with respect to flux measurements from 19 eddy covariance sites over 6 different biomes with diverse aridity levels. Results revealed comparable performances of STIC and SEBS (RMSE of ~ 70 W m⁻²). However, the relatively complex TSEB model produced a higher RMSE of ~ 90 W m⁻². Comparison between STIC ET estimate and the operational ECOSTRESS ET product from NASA PT-JPL model showed a difference in RMSE between the two ET products around 50 W m⁻². Substantial overestimation (>80 W m⁻²) was noted in PT-JPL ET estimates over shrublands and savannas presumably due to the weak constraint of LST in the model. Overall, the EEH is promising to serve as a support to the Land Surface Temperature Monitoring (LSTM) mission.

1 Introduction

Evapotranspiration (ET) is an intrinsic component of climate in the land-atmosphere system and plays a critical role in affecting turbulence, cloud formation and convection at the local scale (Chen and Liu 2020; Fisher et al. 2017). As an important component of the water cycle in the terrestrial ecosystems, it quantifies the amount of water loss from the Earth surface to atmosphere (Chen and Liu 2020; Jasechko et al. 2013). ET consists of evaporation from soil (or water bodies) and wet vegetation and transpiration through pores in plant leaves. Through the stomatal conductance, transpiration is closely related to CO₂ exchange between leaf and atmosphere (Anderson et al. 2008). Thus, ET links the land surface water, energy, and carbon cycles (Anderson et al. 2008; Fisher et al. 2017; Mallick et al. 2021), and is a keystone variable in terrestrial ecosystem processes (Bai et al. 2022; Bayat et al. 2018; Kustas and Anderson 2009; Ryu et al. 2011).

Thermal infrared (TIR) remote sensing has been widely used to obtain ET at large scales considering land surface temperature (LST) constrains the magnitude and variability of the surface energy balance (SEB) components and is immensely sensitive to evaporative cooling (Crago and Qualls 2014; Mallick et al. 2021; Mallick et al. 2014; Norman et al. 1995). ET products are generated from TIR observations of different sensors, including Landsat (Anderson et al. 2012; Anderson et al. 2021; Jaafar et al. 2022), Moderate resolution Imaging Spectroradiometer (MODIS) (Chen et al. 2019; Chen et al. 2021; Senay et al. 2013), Visible Infrared Imaging Radiometer Suite (VIIRS) onboard polar-orbiting satellites (Jaafar et al. 2022), and Advanced Baseline Imager (ABI) (Anderson et al. 2007; Fang et al. 2019) onboard Geostationary Operational Environmental Satellite (GOES). These ET data are harnessed in a variety of applications such as drought monitoring (Anderson et al. 2011; González-Dugo et al. 2021; Otkin et al. 2013), water resource management (Anderson et al. 2012), irrigation control (Allen et al. 2011), global change studies (Dai et al. 2004; Mao et al. 2015), and biodiversity assessments (Fisher et al. 2011).

However, there remains a gap in retrieving ET with concurrently high spatial and temporal resolutions at the global scale. For the polar-orbiting satellites, the Landsat ET product has a high spatial resolution (30 m via thermal sharpening) but coarse temporal resolution (16 days). MODIS and VIIRS have a daily temporal resolution but coarse spatial resolution (≥ 500 m). For the geostationary satellites, the diurnal cycle can be captured by the sub-hourly observations, but the spatial resolution is above 1 km due to the orbit altitude and spatial coverage is limited to the continental scale. This constrains subsequent applications of ET products.

The ECOsystem Spaceborne Thermal Radiometer Experiment on Space Station (ECOSTRESS), positioned on the International Space Station (ISS) on 29 June 2018, is a pathfinder for the next generation TIR missions (Fisher et al. 2020; Hook et al. 2019; Hulley et al. 2021). It collects thermal images in five bands between 8 and 12.5 μm with a high spatio-temporal resolution at varying times of the day. The spatial coverage is between $\pm 52^\circ$ latitude over the globe. The pixel size after resampling at the nadir is $\sim 70 \times 70$ m. The average revisit time is approximately 1-5 days, depending on the latitude (Xiao et al. 2021). Over high latitude regions where the ISS orbital direction shifts, the observation frequency can reach several times in a single day. Therefore, the ECOSTRESS data provides an unprecedented opportunity for monitoring terrestrial ecosystems (Fisher et al. 2020; Liu et al. 2021; Xiao et al. 2021).

The European ECOSTRESS Hub (EEH) is a project funded by the European Space Agency (ESA), targeted at generating high spatio-temporal resolution LST and ET products over Europe and Africa from ECOSTRESS observations. Three structurally contrasting SEB models were selected to produce ET estimates, i.e., one-source Surface Energy Balance System (SEBS) and Two Source Energy Balance (TSEB) parametric models, and the one-source Surface Temperature Initiated Closure (STIC) analytical model. The EEH LST estimates were used as the driving force for ET retrieval from the three models, with the support of ancillary meteorological data and variables describing the surface conditions (e.g., albedo, vegetation coverage). The uniform forcing data describing the lower boundary conditions enables a fair comparison across a wide spectrum of energy and water availability scenarios among the three models with different parameterization schemes. EEH LST and ET products between August 2018 and December 2021 can be downloaded from the Food Security-TEP portal (<https://foodsecuritytep.net/>). More information about EEH can be found on the landing page (<http://isp-projects.private.list.lu/eeh/public/>).

In this paper, we aimed to evaluate the three ECOSTRESS ET products generated in EEH at the continental scale. A two-step evaluation strategy was adopted. First, the EEH ET products were compared with flux measurements from 19 eddy covariance sites over Europe between 2018 and 2019. Then, the best performing EEH ET product was compared with the official National Aeronautics and Space Administration (NASA) ECOSTRESS ET product retrieved using the PT-JPL model. The purpose of this study is two-fold: 1) providing insights into ECOSTRESS ET products generated using SEB models with different structures and parameterizations schemes, 2) supporting ET retrieval for the future thermal missions like ESA's Land Surface Temperature Monitoring (LSTM) (Koetz et al. 2019), the Franco-Indian joint Thermal infraRed Imaging Satellite for High-resolution Natural resource Assessment (TRISHNA) (Lagouarde et al. 2018) and NASA's Surface Biology and Geology (SBG) (Cawse-Nicholson et al. 2021).

2 ET models in EEH

ET is intrinsically associated with the SEB equation, which is based on the partitioning of net available energy into sensible and latent heat fluxes. The SEB equation is written as follows

$$R_N = \lambda E + H + G \quad (1)$$

where R_N is the net radiation, H and λE are sensible and latent heat fluxes (W m^{-2}), respectively, and G is the ground heat conduction flux. The segregation of net available energy ($R_N - G$) into the two different convective fluxes (H and λE) depends on the land surface moisture status, atmospheric conditions in the lower boundary layer, and biophysical control of vegetation (Anderson et al. 2008; Kustas and Anderson 2009; Mallick et al. 2014; Mallick et al. 2018a; Mallick et al. 2018b).

Most thermal-based ET models calculate ET as a residual of SEB after estimating H or estimate evaporative fraction first and derive ET from the net available energy. These models can be broadly characterized as one-source and two-source models based on the conceptualization of the land surface. In the one-source models, the vegetated surface is regarded as a ‘big leaf’ and the evaporating front is assumed to be at the source/sink height, which is in the immediate vicinity of the surface level. Whereas the two-source models assume that the vegetated surface consists of the soil and vegetation components, and the energy fluxes are partitioned between these two components.

2.1 STIC

The one-source STIC model was first proposed by Mallick et al. (2014). STIC is based on the integration of radiometric temperature into the Penman-Monteith (PM) formulation to find the analytical solution of the aerodynamic and surface conductances. To do so, STIC combines an LST-driven water stress index with aerodynamic equations of H and λE and a modified complementary relationship advection-aridity hypothesis (Mallick et al. 2015). The latest version of STIC (Bhattarai et al. 2018; Mallick et al. 2016) combines the Shuttleworth-Wallace sparse canopy formulation model with the PM big-leaf model to calculate the vapour pressure at the source/sink height (Shuttleworth and Wallace 1985).

2.1.1 State equations of STIC

The four state equations are at the core of STIC, which describe aerodynamic and surface conductances (g_A and g_C), aerodynamic temperature (T_0), and evaporative fraction (F_E):

$$g_A = \frac{\phi}{\rho c_p \left[(T_0 - T_A) + \frac{e_0 - e_A}{\gamma} \right]} \quad (2)$$

$$g_C = g_A \frac{e_0 - e_A}{e_0^* - e_0} \quad (3)$$

$$T_0 = T_A + \left(\frac{e_0 - e_A}{\gamma} \right) \left(\frac{1 - F_E}{F_E} \right) \quad (4)$$

$$F_E = \frac{2\alpha s}{2s + 2\gamma + \gamma \frac{g_A}{g_C} (1 + M)} \quad (5)$$

where Φ is the net available energy, ρ is the density of air (kg m^{-3}), c_p is the specific heat of air at constant pressure ($\text{MJ kg}^{-1} \text{K}^{-1}$), γ is the psychrometric constant (hPa K^{-1}), T_A is air temperature at

the reference height, e_0 and e_0^* is the vapor pressure at the source/sink height, e_A is atmosphere vapor pressure, α is the Priestley-Taylor (PT) coefficient, s is the slope of saturation vapour pressure versus temperature curve estimated at T_A , M is the surface moisture availability (between 0 and 1), which is estimated from LST. Based on the four state equations, algebraic closure is not possible due to the involvement of additional unknowns. Therefore, an iterative solution is adopted to estimate the additional unknown variables (e_0^* , e_0 , α and M).

2.1.2 Iterative solution of e_0^* , e_0 , α and M in STIC

From the aerodynamic equation of λE , e_0^* can be expressed as

$$e_0^* = e_A + \frac{\gamma \lambda E (g_A + g_C)}{\rho c_p g_A g_C} \quad (6)$$

Following Shuttleworth and Wallace (1985), the vapour pressure deficit ($D_0 = e_0^* - e_0$) and vapour pressure (e_0) at the source/sink height are expressed as follows:

$$D_0 = D_A + \frac{s\phi - (s + \gamma)\lambda E}{\rho c_p g_A} \quad (7)$$

$$e_0 = e_0^* - D_0. \quad (8)$$

A physical equation of α is expressed as

$$\alpha = \frac{\left[2s + 2\gamma + \gamma \frac{g_A}{g_C} (1 + M)\right] g_C (e_0^* - e_A)}{2s[\gamma(T_0 - T_A)(g_A + g_C) + g_C(e_0^* - e_A)]}. \quad (9)$$

M is expressed as the ratio of the vapour pressure difference to the vapour pressure deficit between the surface and atmosphere as follows

$$M = \frac{e_0 - e_A}{e_0^* - e_A} = \frac{e_0 - e_A}{k(e_s^* - e_A)} = \frac{s_1(T_{0D} - T_D)}{ks_2(T_R - T_D)} \quad (10)$$

where T_{0D} is the dew-point temperature at source/sink height and T_D is the air dew-point temperature, T_R is the radiometric surface temperature, s_1 and s_2 are the psychrometric slopes of the saturation vapour pressure and temperature between the $(T_{0D} - T_D)$ vs. $(e_0 - e_A)$ and $(T_R - T_D)$ vs. $(e_s^* - e_A)$, and k is the ratio between $(e_0^* - e_A)$ and $(e_s^* - e_A)$, as shown in Figure 1. Despite T_0 driving the sensible heat flux, the comprehensive dry-wet signature of the underlying surface due to soil moisture variations is directly reflected in T_R . Thus, T_R in the denominator is directly related to the surface moisture availability (M). In Equation 10, T_{0D} can be calculated as

$$T_{0D} = T_D + \frac{\gamma \lambda E}{\rho c_p g_A s_1}. \quad (11)$$

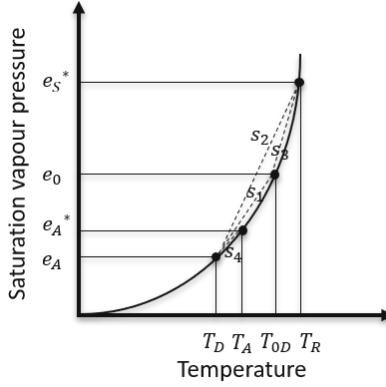


Figure 1. Schematic representation of the exponential relationship between saturation vapor pressure versus temperature.

An iterative method is applied to solve the equations because the four state variables and e_0^* , e_0 , α and M are entangled.

2.1.3 Initialization

An initial value of α is assigned as 1.26 and initial estimates of e_0^* , e_0 are obtained from T_R and M as

$$e_0^* = 6.13753e^{\frac{17.27T_R}{T_R+237.3}} \quad (12)$$

$$e_0 = e_A + M(e_0^* - e_A). \quad (13)$$

M is initialized by assuming $e_0^* = e_s^*$, i.e., k in Equation 10 equals 1, expressed as follows

$$M = \frac{s_1(T_{0D} - T_D)}{s_2(T_R - T_D)}. \quad (14)$$

T_{0D} can be expressed as

$$T_{0D} = \frac{e_s^* - e_A - s_3T_R + s_1T_D}{s_1 - s_3}. \quad (15)$$

The slopes s_1 and s_3 can be expressed as

$$s = 4098 \frac{6.13753e^{\frac{17.27T}{T+237.3}}}{(T + 237.3)^2} \quad (16)$$

where T is set to T_D and T_R for s_1 and s_3 , respectively. With the initial estimates of e_0^* , e_0 , α , and M , g_A , g_C and λE can be calculated. Then e_0^* , e_0 , α and M are updated, and λE is recalculated. The iteration continues until the convergence of λE is achieved.

2.1.4 Hysteresis consideration

By considering the hysteresis between T_R , D_A , and λE , the surface moisture availability M can be expressed as

$$M = \frac{\gamma s_1(T_{0D} - T_D)}{s_3(T_R - T_{0D})s + \gamma s_4(T_A - T_D)}. \quad (17)$$

Hysteresis occurs because the capacity of the soil and vegetation to supply moisture to the atmosphere is larger in the morning than in the afternoon (Boegh et al. 1999). As such, two equations are used for estimating M in STIC depending on the occurrence of hysteresis. It is assumed that Equation 10 is used to indicate surface wetness that controls the evapotranspiration from the upper few centimetres of the surface, whereas Equation 17 is used to indicate the root-zone wetness that controls the evapotranspiration under strong hysteretic conditions between λE , R_N , T_R and D_A .

2.1.5 Driving parameters for STIC

The input variables used for driving the STIC model are listed in Table 1. The LST and emissivity are retrieved from the EEH L2 LST product. The land surface properties including albedo, and land use land cover (LULC) data and fractional vegetation coverage (FVC) are obtained from the Copernicus Global Land Service (CGLS, <https://land.copernicus.eu/global/index.html>). The meteorological data are obtained from the ERA5 reanalysis data (<https://cds.climate.copernicus.eu/cdsapp#!/search?type=dataset>). All these CGLS and ERA5 data are spatially (bilaterally) and temporally (linearly) interpolated to match the ECOSTRESS LST data.

Table 1. Input parameters for STIC, SEBS, and TSEB

| Data | Purpose | Model | Source | Spatial resolution | Temporal resolution |
|--|--------------------------------|------------------|-----------|--------------------|---------------------|
| LST | R_N , T_R | STIC, SEBS, TSEB | ECOSTRESS | ~70 m | daily |
| Emissivity | R_N | STIC, SEBS, TSEB | ECOSTRESS | ~70 m | daily |
| Black sky and white sky albedo (a_{bs} , a_{ws}) | R_N | STIC, SEBS | CGLS | 1 km | 10-day |
| FVC | surface condition | STIC, TSEB | CGLS | 300 m | 10-day |
| NDVI | surface condition | SEBS | CGLS | 300 m | 10-day |
| LAI | surface condition | TSEB | CGLS | 300 m | 10-day |
| LULC | surface condition | STIC, SEBS, TSEB | CGLS | 100 m | annual |
| Shortwave direct radiation (R_{sdir}) | R_N | STIC, SEBS | ERA5 | 0.25° | 1 hour |
| Shortwave global radiation (R_s) | R_N | STIC, SEBS, TSEB | ERA5 | 0.25° | 1 hour |
| Air temperature (T_A) | lower boundary condition (2 m) | STIC, SEBS, TSEB | ERA5 | 0.25° | 1 hour |

| | | | | | |
|--|---------------------------------|------------------|------|-------|--------|
| Atmosphere vapour pressure (e_A) or Dewpoint temperature (T_D) | lower boundary condition (2 m) | STIC, SEBS, TSEB | ERA5 | 0.25° | 1 hour |
| Wind speed | lower boundary condition (10 m) | SEBS, TSEB | ERA5 | 0.25° | 1 hour |

2.2 SEBS

The one-source SEBS model was developed by Su (2002), which also includes sub-models for the roughness length of heat as well as momentum transfer and a formulation for the determination of the evaporative fraction on the basis of energy balance at limiting cases.

To derive the sensible and latent heat fluxes, the similarity theory is used. In the Atmospheric Surface Layer (ASL) similarity relationship, the profiles of the mean wind speed u and the mean temperature $\theta_0 - \theta_a$ can be expressed as follows

$$u = \frac{u_*}{k} \left[\ln \left(\frac{z - d_0}{z_{0m}} \right) - \psi_m \left(\frac{z - d_0}{L} \right) + \psi_m \left(\frac{z_{0m}}{L} \right) \right] \quad (18)$$

$$\theta_0 - \theta_a = \frac{H}{k u_* \rho c_p} \left[\ln \left(\frac{z - d_0}{z_{0h}} \right) - \psi_h \left(\frac{z - d_0}{L} \right) + \psi_h \left(\frac{z_{0h}}{L} \right) \right] \quad (19)$$

where z is the height above the surface (m), $u^* = (\tau_0/\rho)^{1/2}$ is the friction velocity (m s^{-1}), τ_0 is the surface shear stress ($\text{kg m}^{-1} \text{s}^{-2}$), ρ is the density of air (kg m^{-3}), $k = 0.4$ is von Karman's constant, d_0 is the zero plane displacement height (m), z_{0m} is the roughness height for momentum transfer (m), θ_0 is the potential temperature at the surface ($^{\circ}\text{C}$), θ_a is the potential air temperature ($^{\circ}\text{C}$) at height z , z_{0h} is the scalar roughness height for heat transfer (m), ψ_m and ψ_h are the stability correction functions for momentum and sensible heat transfer respectively. L is the Obukhov length, which is defined as follows.

$$L = - \frac{\rho c_p u_*^3 \theta_v}{g H} \quad (20)$$

where g is the acceleration due to gravity (m s^{-2}) and θ_v is the potential virtual temperature near the surface.

The friction velocity, the sensible heat flux and the Obukhov stability length are obtained by solving the system of non-linear Eqs. 18-20. Derivation of the sensible heat flux using the above equations requires only the wind speed and temperature at the reference height as well as the surface temperature and is independent of other SEB terms.

The input parameters used for the SEBS model are listed in Table 1. Most of the input parameters are the same as used for the STIC model, except for two additional parameters. The normalized differential vegetation index (NDVI) data from CGLS are used in the retrieval of leaf area index (LAI) and canopy height. The wind speed from the ERA5 data is used in the retrieval of aerodynamic resistance.

2.3 TSEB

The TSEB model was first proposed by Norman et al. (1995) who represented the surface by a combination of soil and vegetation components. Through the introduction of the TSEB model, the problem of defining the extra resistance (caused by using the radiometric temperature instead of aerodynamic temperature) in the calculation of sensible heat is bypassed.

Component radiometric temperatures are used to compute the surface energy balance fluxes for the canopy and soil components of the combined land surface system:

$$R_{N,S} = H_S + \lambda E_S + G \quad (21)$$

$$R_{N,C} = H_C + \lambda E_C \quad (22)$$

where H_S and H_C are soil and canopy sensible heat fluxes, respectively. λE_S and λE_C are the soil evaporation and canopy transpiration, respectively. G is the soil conduction heat flux, $R_{N,S}$ and $R_{N,C}$ are the net radiation for the soil and canopy components.

By using the series resistance network to account for the interactions between the soil and vegetation canopy fluxes, the sensible heat fluxes can be expressed as follows:

$$H_S = \rho c_p \frac{T_S - T_{AC}}{R_S} \quad (23)$$

$$H_C = \rho c_p \frac{T_C - T_{AC}}{R_X} \quad (24)$$

where R_S and R_X are the aerodynamic resistance from soil surface and total boundary layer aerodynamic resistance of the complete canopy leaves, respectively, T_{AC} is the momentum aerodynamic temperature.

For the latent heat flux from the canopy, the Priestly-Taylor formula is used to initially estimate a potential rate for λE_C

$$\lambda E_C = \alpha_{PT} f_G \frac{s}{s + \gamma} R_{N,C} \quad (25)$$

where α_{PT} is the Priestly-Taylor constant, with the initial value set to 1.3 and a higher value (~2) under well-watered partial canopy cover conditions in advective environments, f_G is the fraction of green vegetation, with the initial value set to 1. Based on λE_C , the initial canopy temperature T_C can be obtained as follows

$$T_C = T_a + \frac{R_{N,C} R_A}{\rho c_p} \left[1 - \alpha_{PT} f_G \frac{s}{s + \gamma} \right] \quad (26)$$

where R_A is the aerodynamic resistance to heat transfer (s/m). The soil component temperature can be calculated based on the ensemble radiometric temperature T_R and T_C . Then the sensible and latent heat fluxes of soil are calculated based on the energy balance.

Non-physical solutions, such as daytime condensation at the soil surface (i.e., $\lambda E_S < 0$), can be obtained under conditions of moisture deficiency. This occurs because the initial value of α_{PT} used for the initiation of λE_C can lead to an overestimation of transpiration in water deficit environments. If this is encountered, α_{PT} is iteratively reduced until λE_S approaches 0.

The input parameters used for the TSEB model are listed in Table 1, which are almost the same as used for SEBS. The canopy height is calculated using the FVC and LULC data by linear scaling between a seasonal minimum and maximum canopy height value for each land surface type (Massman 1997). The uniform driving variables for the three models facilitate a fair and thorough comparison among the three different SEB models.

3 Evaluation method

To evaluate the three EEH ET products, 19 eddy covariance (EC) sites over Europe were selected (Table 2) from the Integrated Carbon Observations System (ICOS) and European Fluxes Database Cluster (EFDC). These sites cover six different biomes, including forest (deciduous broadleaf forest, evergreen needleleaf forest and mixed forest), cropland, grassland, shrubland, wetland and savanna. The instantaneous clear-sky ET estimates (in the form of latent heat flux) were compared against half-hourly latent heat flux measurements closest to the ECOSTRESS overpass times between 2018 and 2019 at the selected sites. A Bowen ratio SEB closure correction was applied to the EC data before the comparison based on the measurements of four components in surface radiation budget, λE , H , and G (Bhattarai et al. 2018). Some extracts were unable to provide all the seven measurements required for the SEB closure correction and thus discarded. Moreover, the extracts were also discarded if any of these seven measurements did not have a good quality (indicated by the quality control flag). Considering the average footprint of the EC sites (Fisher et al. 2020), subsets of 3×3 pixels were extracted centred on the tower coordinates and the average ET values were used in the comparison. To mitigate the uncertainties introduced due to cloud contamination, only extracts surrounded by 15×15 (approximately 1 km) cloud-free pixels (based on the EEH cloud mask product) were considered for further evaluation. The evaluation was first conducted over different land surface types, followed by an overall comparison by gathering the samples at all the sites.

Table 2. List of the selected eddy covariance flux sites. The biomes are according to the IGBP classification, and climate is according to the Köppen climate type. Biomes covered in this study include deciduous broadleaf forest (DBF), evergreen needleleaf forest (ENF), mixed forest (MF), savanna (SAV), cropland (CRO), grassland (GRA), shrubland (SHR) and wetland (WET). Climate types include humid subtropical (Cfa), temperate oceanic (Cfb), hot-summer Mediterranean (Csa), hot-summer humid continental (Dfa), warm-summer humid continental (Dfb), and subarctic (Dfc). Mean annual precipitation (MAP) and aridity index (AI) indicate the aridity level at the sites. AI is calculated as the ratio between precipitation and potential ET for 30 years and indicates the local climatology.

| Site ID | Biome | Climate | Latitude (°) | Longitude (°) | MAP (mm) | AI | Source |
|---------|-------|---------|--------------|---------------|----------|------|--------|
| BE-Lcr | DBF | Cfb | 51.11 | 3.85 | 861 | 0.93 | ICOS |
| BE-Lon | CRO | Cfb | 50.55 | 4.75 | 743 | 0.97 | ICOS |
| BE-Maa | SHR | Cfb | 50.98 | 5.63 | 839 | 0.93 | ICOS |
| BE-Vie | MF | Cfb | 50.31 | 6.00 | 1062 | 1.37 | EFDC |
| CZ-Wet | WET | Dfa | 49.03 | 14.77 | 604 | 0.74 | EFDC |
| DE-Geb | CRO | Cfb | 51.10 | 10.92 | 470 | 0.58 | EFDC |
| DE-Gri | GRA | Dfb | 50.95 | 13.51 | 872 | 0.91 | ICOS |
| DE-Kli | CRO | Dfb | 50.89 | 13.52 | 842 | 1.00 | EFDC |
| DE-Rur | GRA | Cfb | 50.62 | 6.30 | 1033 | 1.38 | EFDC |
| DE-RuS | CRO | Dfb | 50.87 | 6.45 | 698 | 0.82 | ICOS |
| ES-LM1 | SAV | Csa | 39.94 | -5.78 | 700 | 0.30 | EFDC |

| | | | | | | | |
|--------|-----|-----|-------|-------|------|------|------|
| ES-Abr | SAV | Csa | 38.70 | -6.79 | 400 | 0.32 | EFDC |
| FR-Aur | CRO | Cfb | 43.55 | 1.11 | 669 | 0.74 | ICOS |
| FR-Bil | ENF | Cfb | 44.49 | -0.96 | 960 | 0.89 | ICOS |
| FR-Hes | DBF | Cfb | 48.67 | 7.07 | 820 | 0.89 | EFDC |
| FR-LGt | WET | Cfb | 47.32 | 2.28 | 700 | 0.73 | ICOS |
| FR-Mej | GRA | Cfb | 48.12 | -1.80 | 722 | 0.79 | ICOS |
| IT-Lsn | SHR | Cfa | 45.74 | 12.75 | 1100 | 0.91 | ICOS |
| IT-Tor | GRA | Dfc | 45.84 | 7.58 | 945 | 1.42 | ICOS |

284 Three statistical metrics were used to assess the performances of ET products:

$$r = \frac{\sum_{i=1}^n (E_i - \bar{E}) (O_i - \bar{O})}{\sqrt{\sum_{i=1}^n (E_i - \bar{E})^2} \sqrt{\sum_{i=1}^n (O_i - \bar{O})^2}} \quad (27)$$

$$RMSE = \sqrt{\frac{\sum_{i=1}^n (E_i - O_i)^2}{n}} \quad (28)$$

$$bias = \sum_{i=1}^n \frac{E_i - O_i}{n} \quad (29)$$

285 where r is the Pearson's correlation coefficient, $RMSE$ is root-mean-square error, $bias$ is the mean
 286 bias, between the model and measurements, n is the total number of data pairs. E_i and O_i are the
 287 model estimated and measured latent heat fluxes and \bar{O} is the average of observed values and \bar{E} is
 288 the average of estimated values. Additionally, the Kling-Gupta efficiency (KGE) is adopted to
 289 provide a quantitative and objective assessment of the agreement between the measured latent heat
 290 fluxes and ET estimates (Gupta et al. 2009). It is calculated as follows

$$KGE = 1 - \sqrt{(r - 1)^2 + \left(\frac{\sigma_s}{\sigma_0} - 1\right)^2 + \left(\frac{u_s}{u_0} - 1\right)^2} \quad (30)$$

291 where r is the Pearson correlation coefficient, σ_0 and σ_s are the standard deviations of EC site
 292 measurements and EEH estimates, respectively, and u_0 and u_s are the averages of measurements
 293 and estimates, respectively. The closer KGE is to 1, the more consistent the ET estimates are with
 294 the flux measurements.

295 Furthermore, the best performing ET product among the three was compared with the operational
 296 NASA ECOSTRESS ET product generated using the PT-JPL model (Fisher et al. 2020) at the
 297 same EC sites. The three statistical metrics described in Equations 27-29 were also used in the
 298 comparison.

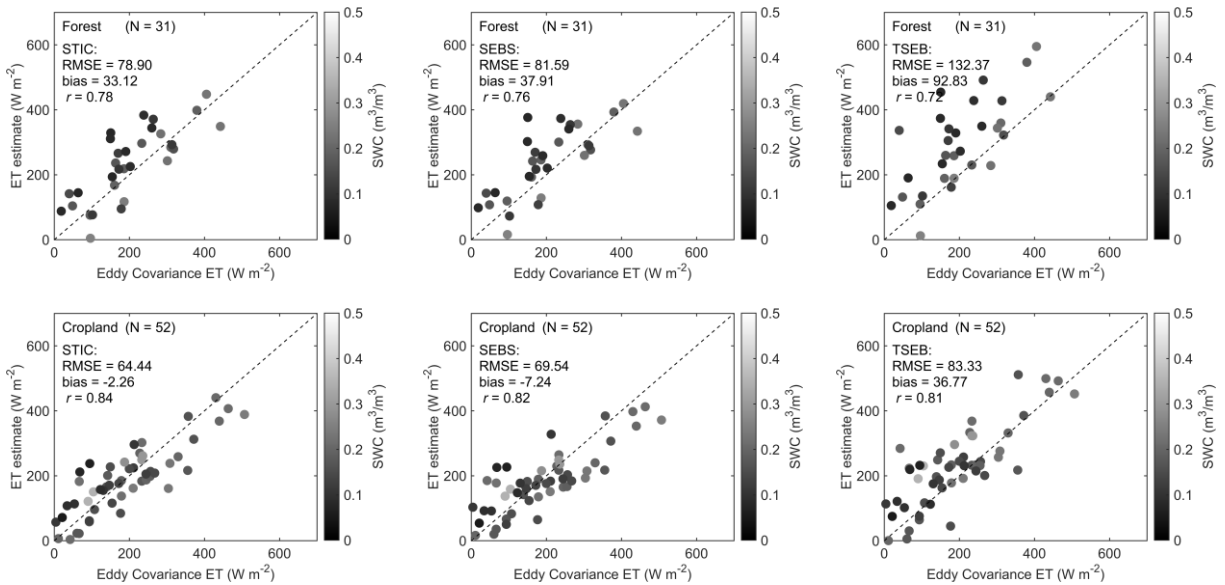
299 4 Results

300 4.1 Model intercomparison

301 Comparison among the three EEH ET products over six different biomes (Figure 2) for a wide
 302 range of soil water content (SWC) reveals that the STIC ET estimates produce the least statistical

errors over forest, cropland, shrubland and savanna (RMSE between 57.21 and 78.90 W m^{-2} , bias between -21.43 and 38.36 W m^{-2}). While the SEBS ET estimates have the highest consistency with respect to EC measurements over grassland and wetland, the performance of SEBS is poor in semiarid shrubland and savanna. SEBS shows the highest RMSE ($\sim 135 \text{ W m}^{-2}$) and bias ($\sim 119 \text{ W m}^{-2}$) in these water-scare ecosystems among the three ET products. In contrast, TSEB ET estimates have the maximum RMSE (between 68.39 and 132.37 W m^{-2}) and bias (between 36.77 and 92.83 W m^{-2}) over most of the land surface types except for shrubland and savanna (RMSE between 60 and 85 W m^{-2} , bias between 10 and 50 W m^{-2}). The performances of STIC and TSEB are comparable over shrubland and savanna, with differences of RMSE and bias within 10 W m^{-2} . Overall, ET estimates from STIC have consistent performances across different biomes. The SEBS ET estimates perform reasonably well in radiation-controlled ecosystems, which is on the contrary to the TSEB estimates.

All the models show relatively higher uncertainties in ET estimates over forest and wetland, where RMSEs are approximately 80 W m^{-2} and biases are above 30 W m^{-2} . The large error in ET estimates over forest is probably partly caused by the inconsistency between the meteorological variables from the ERA5 reanalysis data and the actual conditions at the reference height above the forest. On the contrary, due to the low canopy height and uniform landscape, the atmospheric conditions are better depicted by the meteorological data over grassland and cropland, which leads to a better ET estimation accuracy in these biomes. For the wetland, the high ET errors under high SWC condition could be due to the presence of background water, which does not match the conceptualized surface (soil-vegetation-atmosphere continuum) in the three SEB models. Over savanna, the overestimation by all the models reflects the challenges in estimating ET over semiarid complex landscapes with substantial water stress and low magnitude of ET.



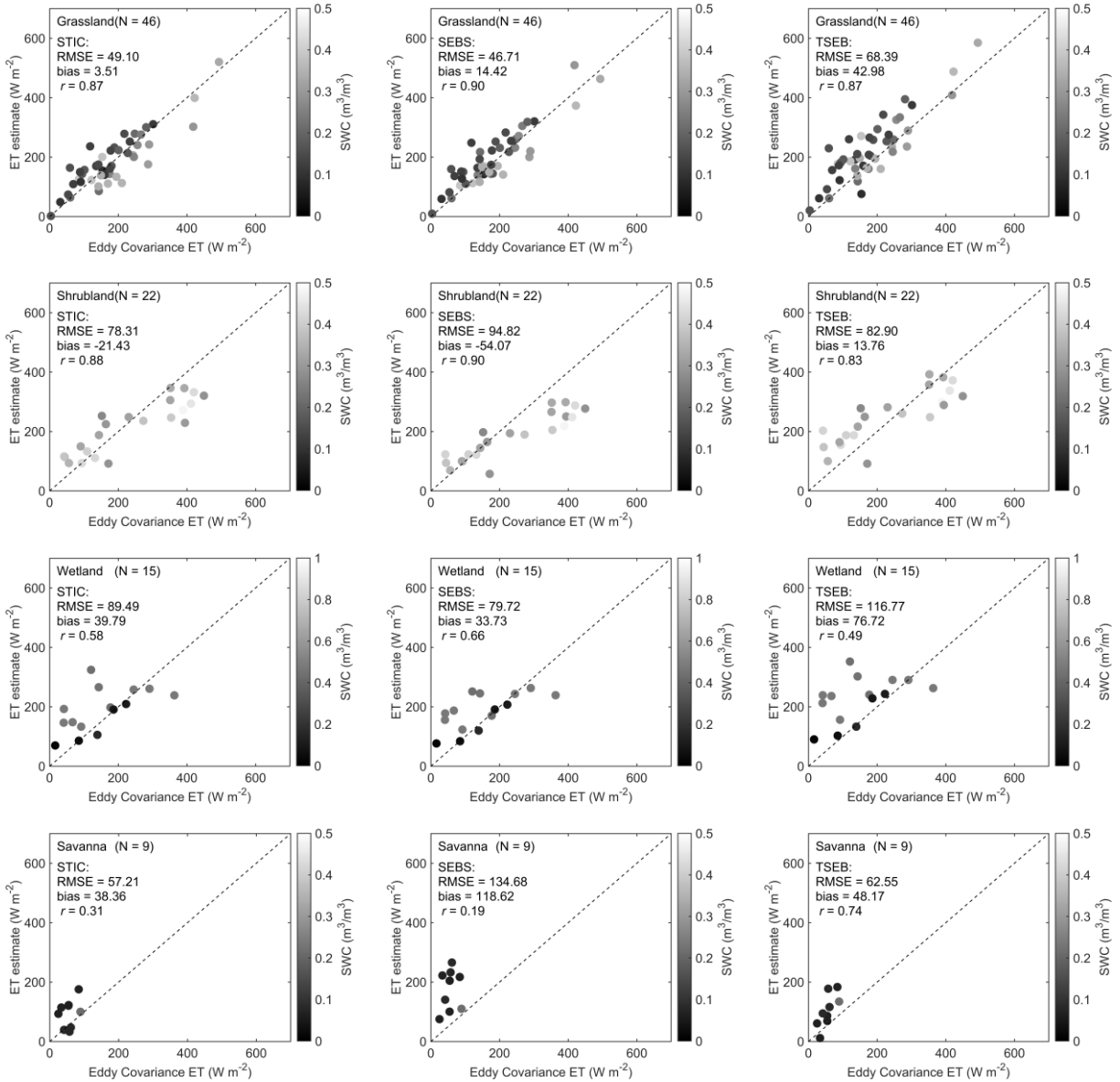
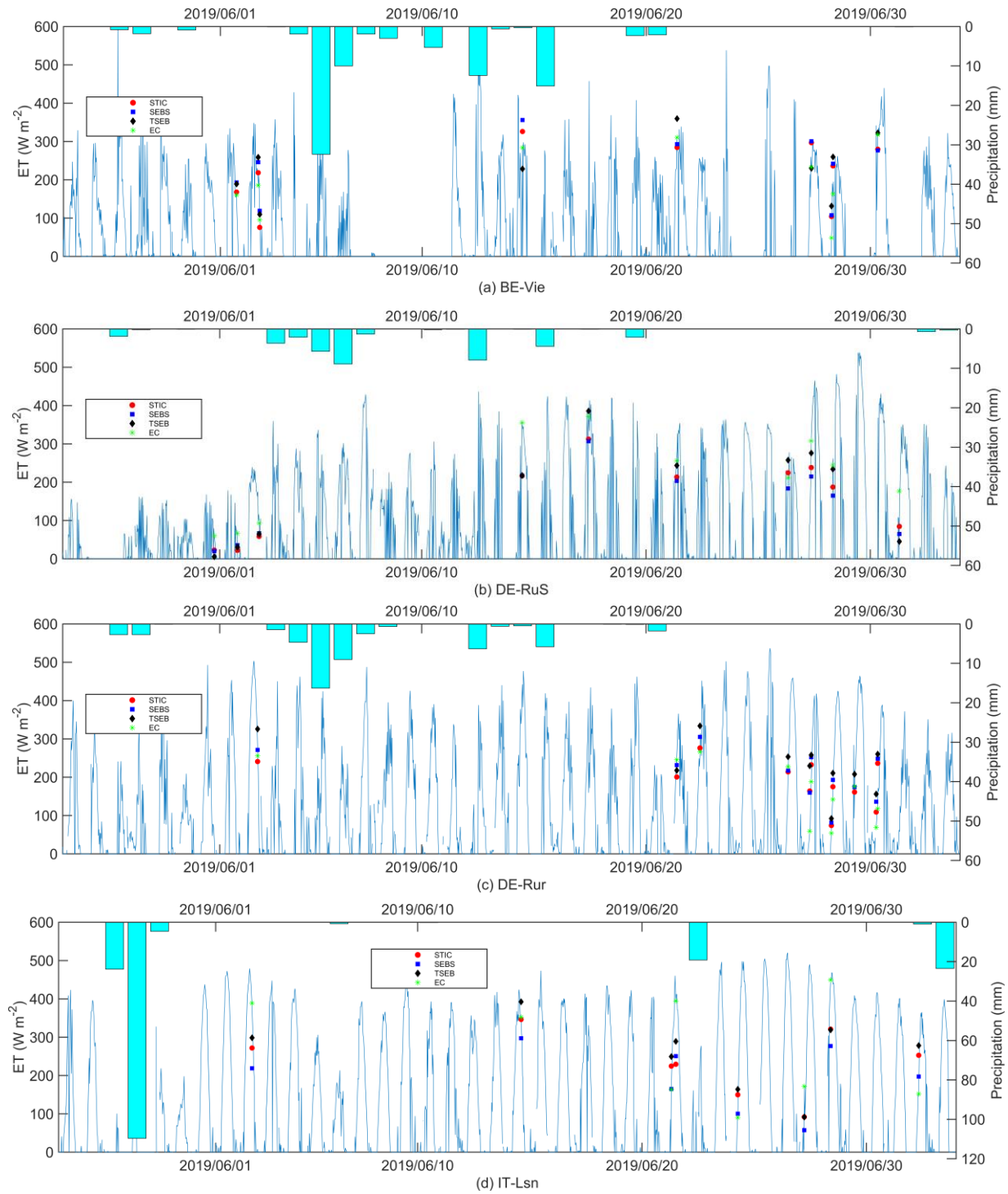


Figure 2. Comparison between the observed ET at EC sites and instantaneous ET estimates from STIC, SEBS and TSEB for 6 biomes during the period 2018–2019. The colour bar represents the soil water content (SWC) measurements from the EC sites.

The time series of EEH ET estimates at six representative biomes is shown in Figure 3. Overall, the ET estimates capture the variation in EC flux measurements although the magnitude is different on some days. The diurnal variation of ET is reasonably represented by the estimates (Figure 3(a) and (c)). The lagged responses of ET to rainfall events are shown. In line with the better performances over grassland and cropland in Figure 2, the EEH ET estimates are also closer to the

334 EC measurements over these two biomes as compared to the other four. The overestimation of the
 335 EEH ET products over savanna is clearly embodied (Figure 3(f)).



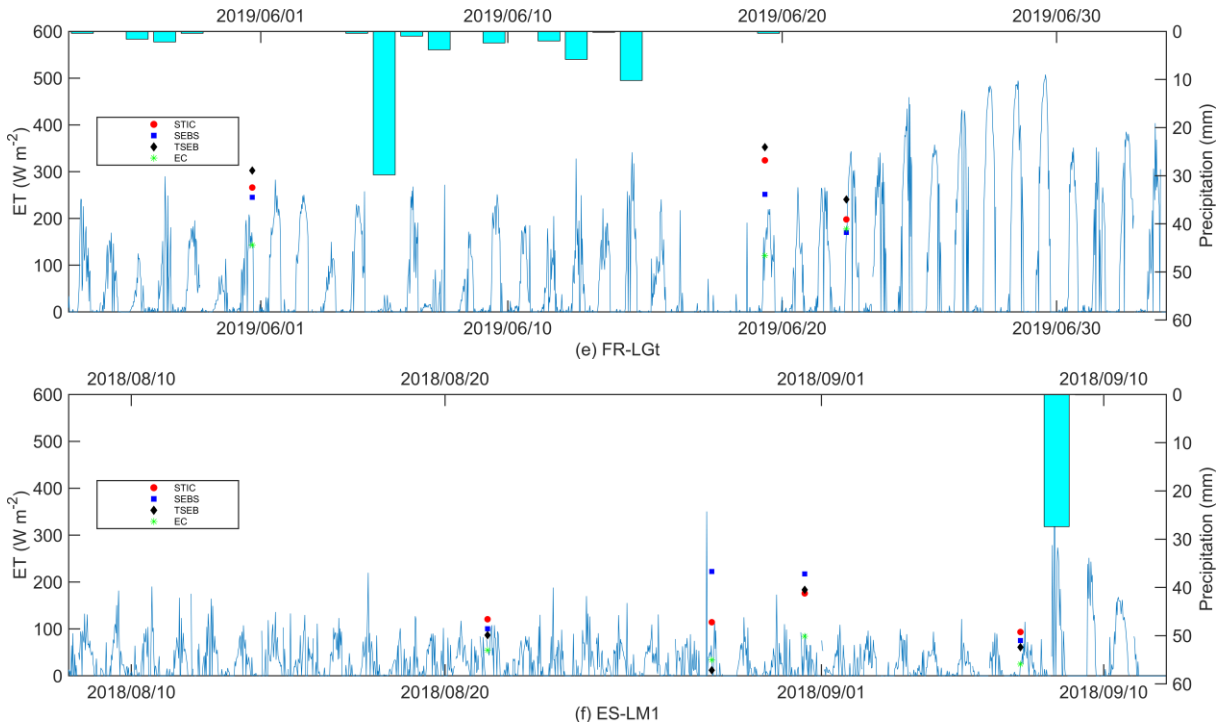


Figure 3. Time series of the observed ET and EEH ET estimates from STIC, SEBS and TSEB at six representative sites of different biomes (a) forest (BE-Vie), (b) cropland (DE-RuS), (c) grassland (DE-Rur), (d) shrubland (IT-Lsn), (e) wetland (FR-LGt), and (f) savanna (ES-LM1). The blue line represents the diurnal cycle of latent heat flux measurements at the EC sites. The bar represents the daily precipitation obtained by accumulating the half-hourly measurements from the EC sites.

Overall, the STIC ET estimates have the lowest statistical errors (Figure 4). The accuracy of SEBS is similar, with an RMSE around 70 W m^{-2} , bias of $\sim 10 \text{ W m}^{-2}$, and correlation coefficient (r) around 0.8. ET estimates from TSEB have a relatively larger RMSE (92.90 W m^{-2}) and bias (49.45 W m^{-2}) although having a similar r (0.77) to the other two models.

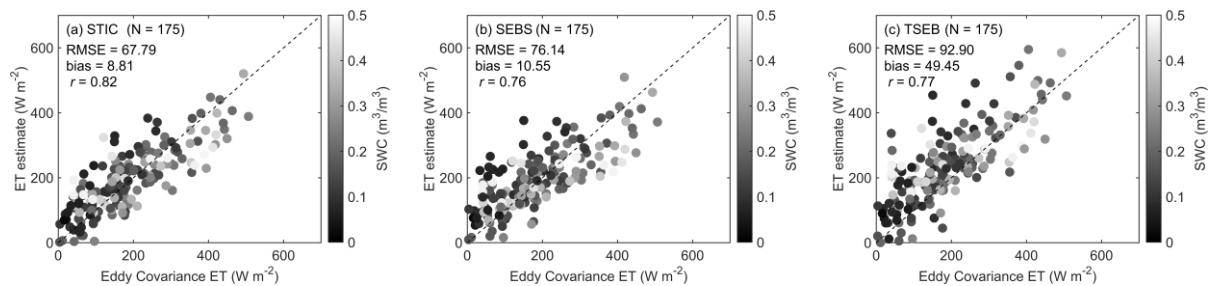


Figure 4. Comparison between the observed ET and EEH ET estimates at all the eddy covariance sites for (a) STIC, (b) SEBS and (c) TSEB during the period between 2018 and 2019. The colour bar represents the SWC measurements from the EC sites.

To understand the model performance under different aridity conditions, the relationship between KGE and aridity index is shown in Figure 5. Aridity index is calculated as the ratio between precipitation and potential ET for 30 years, which indicates the local climatology. Here, the Global

Aridity Index and Potential Evapotranspiration Climate Database v3 (Zomer and Trabucco 2022) (Global-AI_PET_v3) at 1 km pixel scale was used to obtain the aridity indices at the EC sites. The KGE for STIC at most of the sites are close to 1, indicating a good agreement between the ET estimates and EC measurements. Only the two sites over wetland and two sites over savanna are below 0.5, which is consistent with the large biases in these two biomes as found in Figure 2. It is also clear that the accuracy of ET estimates improves when the sites have a humid climate (aridity index >0.65) as compared to those with a semiarid (0.2-0.5) or dry subhumid (0.5-0.65) climate. The SEBS estimates have a similar performance when the aridity index is above 0.5. Whereas KEG is notably lower for SEBS under a semiarid climate. The KGE samples for TSEB are more scattered, and the magnitudes of KGE at most of the sites are lower than STIC and SEBS.

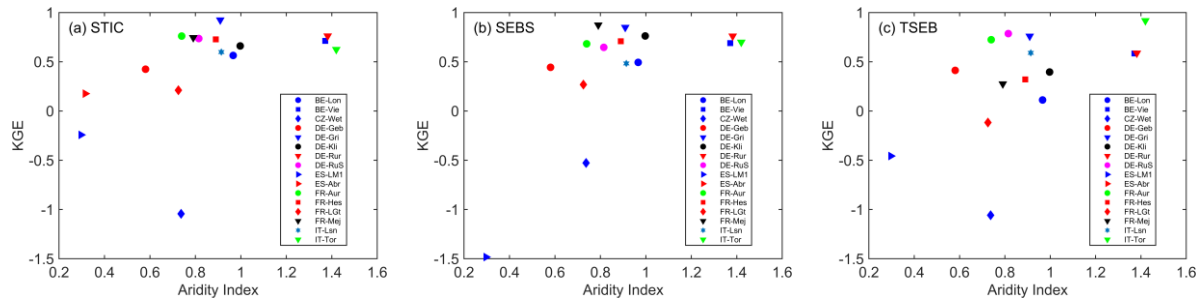
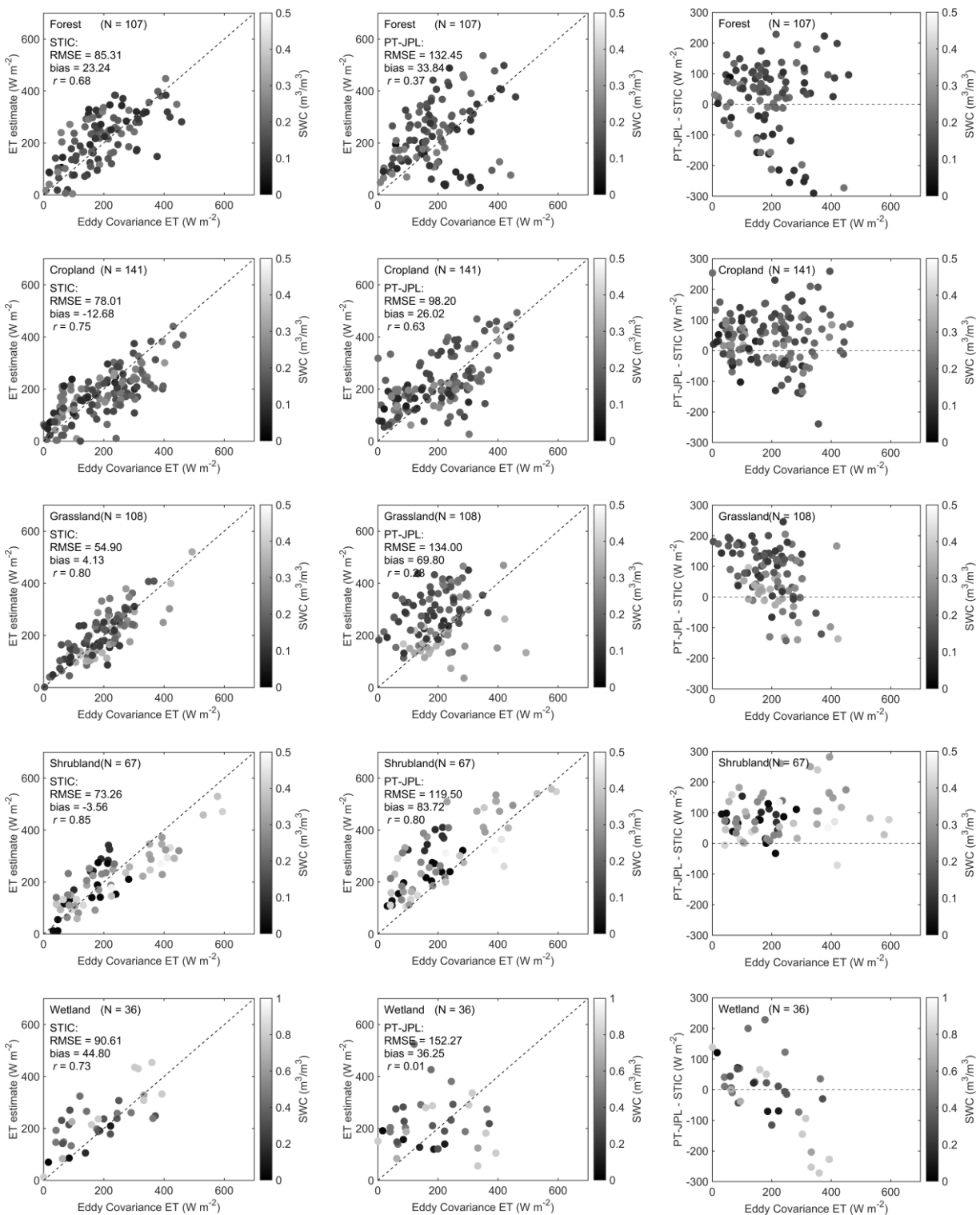


Figure 5. KGE at different aridity levels for various sites for (a) STIC, (b) SEBS and (c) TSEB during the period between 2018 and 2019. Sites over the same land surface type are represented using the same marker. The KEG at ES-Abr for SEBS (-5.07) and TSEB (-2.50) are not shown due to the excessively low values. The higher the aridity index is, the more humid conditions are.

4.2 Comparison between STIC and PT-JPL

Given that the ET estimates from STIC showed the best agreement with the EC measurements, STIC ET was compared with the official ECOSTRESS ET that was generated using the PT-JPL model (Figure 6). The performance of STIC is pronouncedly better as compared to PT-JPL over all the biome types. The differences in RMSE are $\sim 50 \text{ W m}^{-2}$ in all the cases except over cropland where the difference is around 20 W m^{-2} . The PT-JPL ET estimates are scattered, with most samples above the 1:1 line. This is reflected in the large positive biases of PT-JPL estimates. The overestimation of PT-JPL as compared to STIC in dry conditions (with low EC ET) is clearly shown. In particular over shrubland and savanna, all the estimates from PT-JPL are greater than from STIC. We infer that this is caused by the weak LST constraint in the PT-JPL model, which makes the model insensitive to surface water stress. In the PT-JPL model, LST is just used in the calculation of surface net radiation. Whereas in the STIC model, LST is embedded in the calculation of surface soil moisture availability and thus directly linked to evaporative fraction (Equation 5).



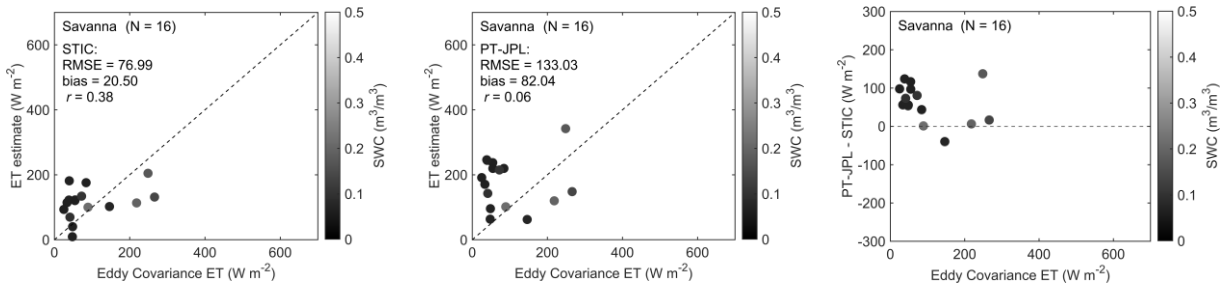


Figure 6. Comparison between the observed ET at EC sites and instantaneous ET estimates from STIC and PT-JPL over 6 land surface types during the period between 2018–2020. The colour bar represents the SWC measurements from the EC sites.

Overall, the PT-JPL model has a RMSE of 123.55 W m^{-2} and bias of 48.54 W m^{-2} , which are both $\sim 50 \text{ W m}^{-2}$ higher than those of STIC. The PT-JPL ET estimates are scattered, in contrast to the STIC estimates that are tightly and evenly distributed around the 1:1 line (Figure 7(a) and (b)). The Taylor diagram further clarifies the closeness of STIC ET estimates to the ground ‘truth’ although the standard deviation of PT-JPL ET estimates is closer to that of the observations.

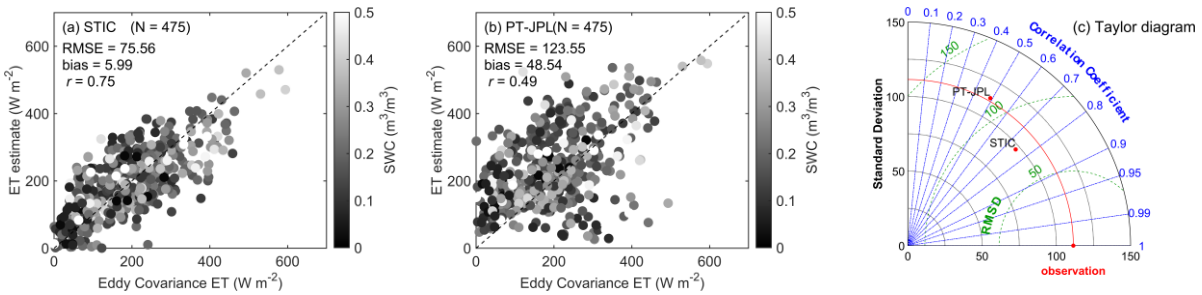


Figure 7. Comparison between the observed ET and instantaneous ET estimates at all the eddy covariance sites for (a) STIC and (b) PT-JPL and (c) Taylor diagram during the period between 2018 and 2020.

5 Discussion

5.1 Factors affecting model performances

Different impact factors influencing the model performances were investigated, including SWC (Figure 8), vapor pressure deficit (VPD, Figure 9), viewing zenith angle (VZA, Figure 10), and FVC (Figure 11), respectively.

For all the models, the variation of ET bias with SWC is exponential (Figure 8). A sharp increase in ET bias with progressive surface drying (decreasing SWC) is evident when SWC is below $0.1 \text{ m}^3 \text{ m}^{-3}$, which is also associated with low ET magnitude. This is particularly obvious for SEBS, which showed a large overestimation under dry conditions. This reflects the challenges as well as opportunities in enhancing the performances of ET models in water-scarce regions where the coupling between the land surface and atmosphere is strong and evaporation is mainly driven by soil water induced stomatal control (Mallick et al. 2022; Mallick et al. 2016). In contrast, when SWC is above $0.2 \text{ m}^3 \text{ m}^{-3}$, the ET bias tends to diminish and approaches zero, although underestimation is indicated when EC ET are high. Due to the scattered samples of TSEB

estimates, the relationship between ET bias and SWC is not so strong ($R^2 = 0.07$) as found in STIC and SEBS. However, the overall trends in ET bias versus SWC are similar in all the three models.

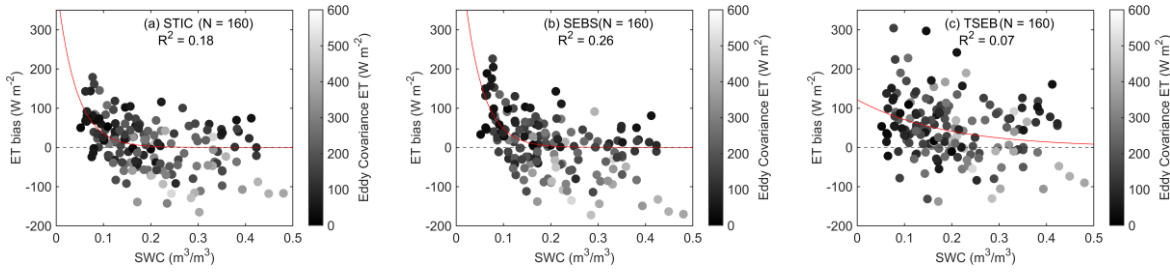


Figure 8. ET bias (ET estimate minus ground measurement) versus SWC for (a) STIC, (b) SEBS and (c) TSEB during the period between 2018 and 2019. Samples at all the sites except for the wetland sites are included. The wetland sites are excluded due to the high SWC and different pattern between ET bias and SWC from the other land surface types.

Compared with SWC, the relationship between ET bias and VPD is not so strong although the bias is generally larger when VPD is above 20 hPa (Figure 9). The increase of ET bias with VPD is more noticeable for SEBS. This is consistent with the large uncertainty of SEBS that could not adequately capture the low ET magnitudes over shrubland and savanna.

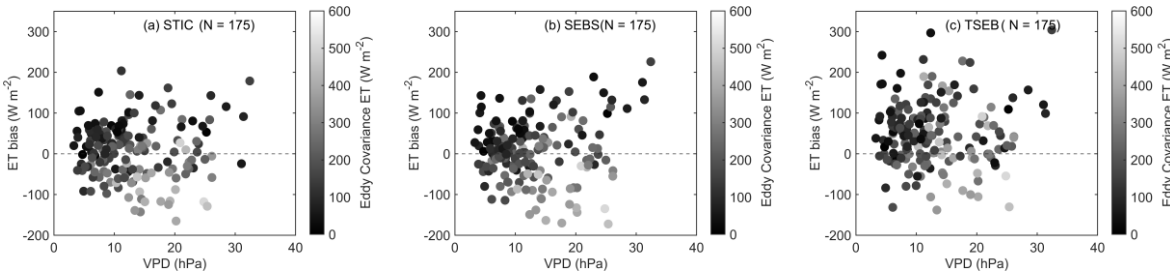


Figure 9. ET bias (ET estimate minus ground measurement) versus VPD for (a) STIC, (b) SEBS and (c) TSEB during the period between 2018 and 2019.

No impact of VZA on ET bias is found for all the three models (Figure 10). The magnitude of ET bias across different VZAs is close. We infer this is partly because the angular variation of thermal radiation is not pronounced when VZA is below 30° (Ermida et al. 2018; Hu et al. 2019; Mwangi et al. 2022). Moreover, the high spatial homogeneity at the EC sites (Fisher et al. 2020) is also an important factor for the weak angular variation of thermal radiation.

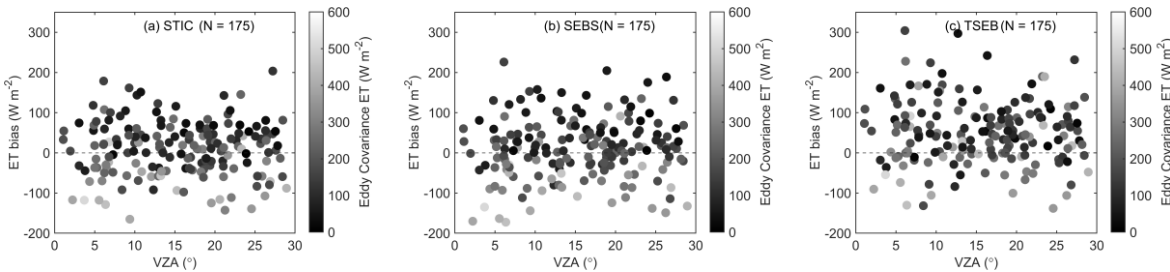


Figure 10. ET bias (ET estimate minus ground measurement) versus VZA for (a) STIC, (b) SEBS and (c) TSEB during the period between 2018 and 2019.

The overestimation of ET over sparsely vegetated surfaces ($FVC < 0.5$) is notable for all the three models (Figure 11). The ET bias of STIC is lower as compared to the other two models, with most of the samples below 100 W m^{-2} . The ET bias of SEBS for $FVC < 0.2$ is substantially higher than STIC and TSEB, which is consistent with the high RMSE of SEBS ET estimates over shrubland and savanna. This is also reported in previous studies (Bhattarai et al. 2018; Boulet et al. 2012; Faivre et al. 2017), which is mostly associated with the underestimation of H due to uncertainties in the estimation of kB^{-1} and z_{OM} when the difference between T_R and T_0 is substantial. Chen et al. (2013) proposed an improved roughness height parameterization by updating kB^{-1} of bare soil, which showed a better performance than the original SEBS model by correcting for the underestimation of H . However, it is beyond the scope of this study to compare the revised SEBS model with the others in detail. For densely vegetated surfaces ($FVC > 0.8$), the ET bias is evenly distributed above and below the zero-bias line. However, the magnitude of bias is higher over densely vegetated surfaces due to the relatively higher ET. For TSEB, high biases in ET are found when FVC approaches unity. This high bias in TSEB is presumably due to the uncertainty in fraction of green vegetation, which is also reflected in the large RMSE of TSEB ET over forests in Figure 2. Given no attempt was made to change the pyTSEB version of Nieto et al. (2016), we adopted the default value of fraction of green vegetation ($=1$) of pyTSEB in EEH. This can be somehow problematic when vegetation senescence occurs. However, accurate retrievals of these vegetation biophysical parameters are difficult to obtain at large spatial scales, especially for ECOSTRESS that only has TIR observations, which could add additional challenges to TSEB. Moreover, the PT-TSEB version with a single PT coefficient was used in the EEH. The PM-TSEB version with tabulated minimum stomatal resistance might mitigate the large uncertainties of TSEB over densely vegetated surfaces (Colaizzi et al. 2014).

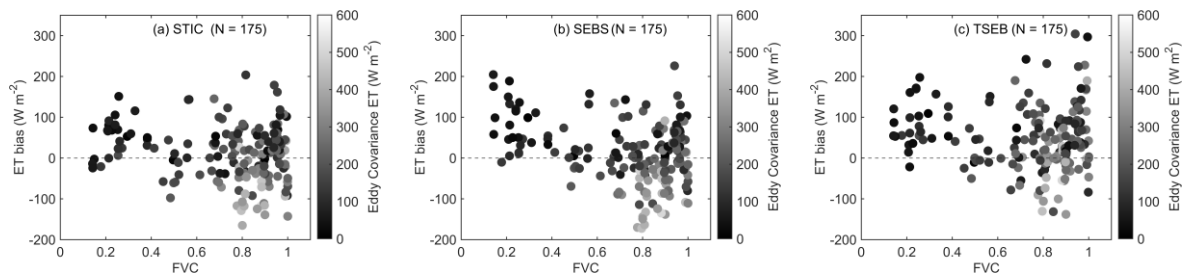


Figure 11. ET bias (ET estimate minus ground measurement) versus FVC for (a) STIC, (b) SEBS and (c) TSEB during the period between 2018 and 2019.

5.2 Contrasting performances of ECOSTRESS ET products

The STIC ET estimates showed consistent performances over different land surface types. This could be attributed to the non-parameterized structure of this model. Different from the other thermal based models, the aerodynamic and surface resistances in STIC are expressed through physical equations without empirical parameterization of surface roughness and atmospheric stability corrections. However, the calculation of aerodynamic resistance relies on wind speed in SEBS and TSEB, which makes these models relatively more sensitive to uncertainties associated with wind velocity. Moreover, the aerodynamic temperature is directly retrieved in STIC instead of utilizing the radiometric temperature as a proxy and involving subsequent empirical corrections as commonly conducted in one-source models (Mallick et al. 2022). As a result, the dependence of ET estimates on additional inputs (e.g., wind speed and canopy height) is also eliminated in STIC. LST is mainly used for depicting surface water availability in STIC rather than directly

calculating sensible heat flux. Considering the current validation datasets, the STIC model is relatively robust across varying biomes.

The SEBS ET estimates showed similar accuracy to the STIC estimates in all cases except for over sparsely vegetated surfaces (i.e., shrubland and savanna). This could be associated with empirical parameterizations of resistances to accommodate the inequality between radiometric temperature and aerodynamic temperature (Mallick et al. 2022; Trebs et al. 2021). Over sparse canopies, large uncertainties exist in the parameterization scheme. Bhattarai et al. (2018) and Trebs et al. (2021) reported that uncertainties in kB^{-1} greatly hindered the accuracy of ET estimates in the arid and semiarid ecosystems. Moreover, there is no universal methodology for calculating the heat roughness length, which varies with vegetation structure, surface water stress and climatic conditions (Kustas and Anderson 2009; Mallick et al. 2022). As such, the SEBS model should be used with caution in operational ET retrieval.

The TSEB ET estimates had larger uncertainties overall as compared to STIC and SEBS. Over forests, the RMSE and bias reached 132.37 and 92.83 W m⁻², respectively. As reported by Yang et al. (2015), a major factor is the uncertainty in determining the initial P-T coefficient, which represents the aerodynamic forcing and vegetation controls on ET. We used the value of 1.26 in the model implementation. However, the P-T coefficient has strong spatial variations with surface dryness, VPD, wind speed and canopy biophysical properties. Thus, a deterministic P-T coefficient can lead to uncertainties at large scales. An adjustment of the initial P-T coefficient based on land surface type may mitigate the uncertainty in ET estimates (Andreu et al. 2018; Cristóbal et al. 2020; Cristóbal et al. 2017; Guzinski et al. 2013). Also, the soil aerodynamic resistance parameterization and the associated empirical coefficients could be another reason (Li et al. 2019). Moreover, the determination of fraction of green vegetation was simplified in EEH and set to 1 directly. This could also contribute to the large uncertainties of TSEB ET estimates considering the import role of canopy biophysical parameters in heat transfer (Kustas et al. 2016). A possible solution could be estimating f_G based on the empirical approach proposed by Fisher et al. (2008). In this case, additional input parameters are required such as fraction of absorbed photosynthetically active radiation (fAPAR), which will bring extra complexity in operational ET retrieval. Although the biophysical parameters (e.g., LAI and FVC) used in TSEB are the same as in STIC and SEBS, the TSEB ET estimates seem to be more susceptible to uncertainties in these biophysical inputs due to the model structure and partitioning of energy between soil and vegetation. Due to the absence of visible and shortwave infrared (VSWIR) bands in the ECOSTRESS observations, external biophysical parameters were used in the ET retrieval. However, the temporal and spatial mismatches between these biophysical parameters and the instantaneous ECOSTRESS LST estimates could have introduced errors into the TSEB ET results (Anderson et al. 2021).

The accuracy of PT-JPL ET estimates was substantially lower as compared to the STIC estimates over all the land surface types. This could be attributed to the following reasons. First, the ECOSTRESS LST is only used for calculating surface net radiation in PT-JPL ET retrieval. Net radiation has a weak dependence on LST and therefore the ET products generated using PT-JPL does not take full advantage of surface water stress information embodied in LST. Second, PT-JPL relies on atmospheric vapor pressure deficit instead of LST for constraining the ET components. Moreover, the determination of the P-T coefficient for different biomes is a challenge as well as a major source of uncertainties. Thus, a physically based formula is needed to estimate

the P-T coefficient for better interpolation of the aerodynamic forcing and soil-vegetation control in the SEB process.

5.3 Uncertainties and limitations in the current evaluation

Although we selected EC sites with good maintenance and only used good quality flux measurements, uncertainties could still exist in the measured fluxes, which may have influenced the evaluation results. Due to the unavailability of well-maintained EC sites over Africa, we only evaluated the EEH ET products over Europe. Also, sites in semiarid regions (e.g., over savanna) have limited sample numbers due to the sparse spatial coverage of ECOSTRESS over the Iberian Peninsula. Inclusion of more EC sites over Africa and semiarid regions in Europe would benefit a more thorough and comprehensive evaluation of EEH ET products in the future.

In the ECOSTRESS observations, only five thermal bands (three since May 2019 due to the loss of the two onboard Mass Storage Units) are available. Therefore, ancillary data related to land surface biophysical properties can only be obtained from external sources. In the case of EEH, we used the CGLS FVC, and albedo data generated from Sentinel-3/OLCI and PROBA-V. Therefore, discrepancies in spatial resolution and satellite overpass times cannot be avoided, which could impact the ET retrieval process. Moreover, cloud masking without the support of VSWIR bands is challenging and problematic. Although strict cloud screening was exercised in the evaluation, residuals from the cloud mask could still harm the accuracy of LST retrieval, thus impacting ET estimation. Fortunately, in the future thermal missions such as TRISHNA and LSTM, these problems will be minimized substantially with the measurement in VSWIR bands. Correspondingly, the accuracy of ET estimates can be envisaged to further improve.

Due to the issue with the sensor's radiometric calibration in Collection 1 ECOSTRESS data, a cold bias of ~1 K was found in the ECOSTRESS LST products (Hulley et al. 2021). This has been addressed in Collection 2 that will be released in 2022. Accordingly, we will reprocess the ECOSTRESS LST, and ET products based on the Collection 2 ECOSTRESS radiance data and extend the temporal coverage of EEH products to September 2023 in the Phase-2 of EEH. The 5-year time series of high spatio-temporal resolution ECOSTRESS products with improved accuracy is expected to greatly benefit the studies on terrestrial ecosystem processes.

6 Conclusion

TIR observations from ECOSTRESS onboard the ISS with high spatio-temporal resolution provide a good opportunity for generating LST and ET products at the field scale over the globe. In this study, we evaluated three ECOSTRESS ET products generated in the EEH project based on three structurally contrasting thermal-based SEB models (i.e., STIC, SEBS, and TSEB). The ET estimates were compared against latent heat flux measurements at 19 EC sites over Europe between 2018 and 2019. Furthermore, the best performing STIC ET estimates were compared with the NASA official ECOSTRESS ET products using the PT-JPL model at the same sites. Six different land surface types were encompassed in the evaluation, including forest, grassland, cropland, shrubland, wetland and savanna.

The results revealed that the STIC ET estimates had consistent performance over different land surface types with a relatively better accuracy as compared to the other two models, which is

directly linked to the analytical framework of STIC without resistance parameterizations. The SEBS estimates had similar performances to STIC except over shrubland and savanna where the uncertainties of SEBS ET were substantially higher than for the other two models. This is attributed to the large uncertainties in empirical parameterizations of resistances to accommodate the inequality between radiometric temperature and aerodynamic temperature in SEBS over sparsely vegetated surfaces. The performance of TSEB was particularly good in water-scarce ecosystems. However, large uncertainties were found in TSEB in radiation-controlled ecosystems. The setting of P-T coefficient, soil aerodynamic resistance parameterization, fraction of green vegetation values, and temporal and spatial mismatches between the input biophysical parameters and the instantaneous ECOSTRESS LST retrievals could account for the high uncertainties to some extent.

Compared with the PT-JPL estimates, the performance of STIC was substantially better over all the land surface types. The overall RMSE and bias were both $\sim 50 \text{ W m}^{-2}$ higher in the PT-JPL estimates than those of STIC. The serious overestimation of PT-JPL ET estimates could be explained by the weak LST constraint in the model.

We conclude that the high spatio-temporal resolution EEH ET products provide an unprecedented opportunity for environmental and agricultural applications. The comprehensive evaluation among the EEH ET estimates driven by uniform forcing data provides insights into SEB models with different structures and contrasting parameterization schemes. Overall, the EEH is promising to serve as a support for the future thermal missions such as TRISHNA jointly collaborated by France and India, SBG from NASA and LSTM from ESA.

Acknowledgments

The authors wish to extend their gratitude to all the scientists involved in the ECOSTRESS mission and ground measurement collection in ICOS and EFDC. We would like to thank Dr. Hector Nieto and Dr. Johannes van der Kwast for the open-source Python codes of TSEB (<https://github.com/hectornieto/pyTSEB>) and SEBS (<https://github.com/jvdkwast/PySEBS>), respectively. The manuscript is greatly benefited from the comments and advice from Dr. Dennis Baldocchi and Dr. William P. Kustas on the interpretation of the TSEB ET estimates. The study was conducted under the European ECOSTRESS Hub project (EEH, Contract No. 4000129873/20/I-NS), funded by the European Space Agency (ESA) Earth Observation Envelope Programme (EOEP). Part of this research was carried out at the Jet Propulsion Laboratory, California Institute of Technology, under a contract with the National Aeronautics and Space Administration (80NM0018D0004). K. M. acknowledges the Mobility Fellowship from the FNR Luxembourg (INTER/MOBILITY/2020/14521920/MONASTIC).

References

- Allen, R.G., Pereira, L.S., Howell, T.A., & Jensen, M.E. (2011). Evapotranspiration information reporting: I. Factors governing measurement accuracy. *Agricultural Water Management*, 98, 899-920
- Anderson, M.C., Allen, R.G., Morse, A., & Kustas, W.P. (2012). Use of Landsat thermal imagery in monitoring evapotranspiration and managing water resources. *Remote Sensing of Environment*, 122, 50-65

- Anderson, M.C., Hain, C., Wardlow, B., Pimstein, A., Mecikalski, J.R., & Kustas, W.P. (2011). Evaluation of drought indices based on thermal remote sensing of evapotranspiration over the continental United States. *Journal of Climate*, 24, 2025-2044
- Anderson, M.C., Norman, J.M., Kustas, W.P., Houborg, R., Starks, P.J., & Agam, N. (2008). A thermal-based remote sensing technique for routine mapping of land-surface carbon, water and energy fluxes from field to regional scales. *Remote Sensing of Environment*, 112, 4227-4241
- Anderson, M.C., Norman, J.M., Mecikalski, J.R., Otkin, J.A., & Kustas, W.P. (2007). A climatological study of evapotranspiration and moisture stress across the continental United States based on thermal remote sensing: 1. Model formulation. *Journal of Geophysical Research: Atmospheres*, 112
- Anderson, M.C., Yang, Y., Xue, J., Knipper, K.R., Yang, Y., Gao, F., Hain, C.R., Kustas, W.P., Cawse-Nicholson, K., & Hulley, G. (2021). Interoperability of ECOSTRESS and Landsat for mapping evapotranspiration time series at sub-field scales. *Remote Sensing of Environment*, 252, 112189
- Andreu, A., Kustas, W.P., Polo, M.J., Carrara, A., & González-Dugo, M.P. (2018). Modeling surface energy fluxes over a dehesa (oak savanna) ecosystem using a thermal based two-source energy balance model (TSEB) I. *Remote Sensing*, 10, 567
- Bai, Y., Bhattarai, N., Mallick, K., Zhang, S., Hu, T., & Zhang, J. (2022). Thermally derived evapotranspiration from the Surface Temperature Initiated Closure (STIC) model improves cropland GPP estimates under dry conditions. *Remote Sensing of Environment*, 271, 112901
- Bayat, B., van der Tol, C., & Verhoef, W. (2018). Integrating satellite optical and thermal infrared observations for improving daily ecosystem functioning estimations during a drought episode. *Remote Sensing of Environment*, 209, 375-394
- Bhattarai, N., Mallick, K., Brunsell, N.A., Sun, G., & Jain, M. (2018). Regional evapotranspiration from an image-based implementation of the Surface Temperature Initiated Closure (STIC1. 2) model and its validation across an aridity gradient in the conterminous US. *Hydrology and Earth System Sciences*, 22, 2311-2341
- Boegh, E., Soegaard, H., Hanan, N., Kabat, P., & Lesch, L. (1999). A remote sensing study of the NDVI-Ts relationship and the transpiration from sparse vegetation in the Sahel based on high-resolution satellite data. *Remote Sensing of Environment*, 69, 224-240
- Boulet, G., Olioso, A., Ceschia, E., Marloie, O., Coudert, B., Rivalland, V., Chirouze, J., & Chehbouni, G. (2012). An empirical expression to relate aerodynamic and surface temperatures for use within single-source energy balance models. *Agricultural and Forest Meteorology*, 161, 148-155
- Cawse-Nicholson, K., Townsend, P.A., Schimel, D., Assiri, A.M., Blake, P.L., Buongiorno, M.F., Campbell, P., Carmon, N., Casey, K.A., & Correa-Pabón, R.E. (2021). NASA's surface biology and geology designated observable: A perspective on surface imaging algorithms. *Remote Sensing of Environment*, 257, 112349
- Chen, J.M., & Liu, J. (2020). Evolution of evapotranspiration models using thermal and shortwave remote sensing data. *Remote Sensing of Environment*, 237, 111594
- Chen, X., Su, Z., Ma, Y., & Middleton, E.M. (2019). Optimization of a remote sensing energy balance method over different canopy applied at global scale. *Agricultural and Forest Meteorology*, 279, 107633
- Chen, X., Su, Z., Ma, Y., Trigo, I., & Gentile, P. (2021). Remote sensing of global daily evapotranspiration based on a surface energy balance method and reanalysis data. *Journal of Geophysical Research: Atmospheres*, 126, e2020JD032873

- Chen, X., Su, Z., Ma, Y., Yang, K., Wen, J., & Zhang, Y. (2013). An improvement of roughness height parameterization of the Surface Energy Balance System (SEBS) over the Tibetan Plateau. *Journal of Applied Meteorology and Climatology*, 52, 607-622
- Colaizzi, P.D., Agam, N., Tolk, J.A., Evett, S.R., Howell, T.A., Gowda, P.H., O'Shaughnessy, S.A., Kustas, W.P., & Anderson, M.C. (2014). Two-source energy balance model to calculate E, T, and ET: Comparison of Priestley-Taylor and Penman-Monteith formulations and two time scaling methods. *Transactions of the ASABE*, 57, 479-498
- Crago, R.D., & Qualls, R.J. (2014). Use of land surface temperature to estimate surface energy fluxes: Contributions of Wilfried Brutsaert and collaborators. *Water Resources Research*, 50, 3396-3408
- Cristóbal, J., Prakash, A., Anderson, M.C., Kustas, W.P., Alfieri, J.G., & Gens, R. (2020). Surface energy flux estimation in two Boreal settings in Alaska using a thermal-based remote sensing model. *Remote Sensing*, 12, 4108
- Cristóbal, J., Prakash, A., Anderson, M.C., Kustas, W.P., Euskirchen, E.S., & Kane, D.L. (2017). Estimation of surface energy fluxes in the Arctic tundra using the remote sensing thermal-based Two-Source Energy Balance model. *Hydrology and Earth System Sciences*, 21, 1339-1358
- Dai, A., Trenberth, K.E., & Qian, T. (2004). A global dataset of Palmer Drought Severity Index for 1870–2002: Relationship with soil moisture and effects of surface warming. *Journal of Hydrometeorology*, 5, 1117-1130
- Ermida, S.L., Trigo, I.F., DaCamara, C.C., & Roujean, J.-L. (2018). Assessing the potential of parametric models to correct directional effects on local to global remotely sensed LST. *Remote Sensing of Environment*, 209, 410-422
- Faivre, R., Colin, J., & Menenti, M. (2017). Evaluation of methods for aerodynamic roughness length retrieval from very high-resolution imaging lidar observations over the Heihe Basin in China. *Remote Sensing*, 9, 63
- Fang, L., Zhan, X., Schull, M., Kalluri, S., Laszlo, I., Yu, P., Carter, C., Hain, C., & Anderson, M. (2019). Evapotranspiration data product from NESDIS GET-D system upgraded for GOES-16 ABI observations. *Remote Sensing*, 11, 2639
- Fisher, J.B., Lee, B., Purdy, A.J., Halverson, G.H., Dohlen, M.B., Cawse-Nicholson, K., Wang, A., Anderson, R.G., Aragon, B., & Arain, M.A. (2020). ECOSTRESS: NASA's next generation mission to measure evapotranspiration from the international space station. *Water Resources Research*, 56, e2019WR026058
- Fisher, J.B., Melton, F., Middleton, E., Hain, C., Anderson, M., Allen, R., McCabe, M.F., Hook, S., Baldocchi, D., & Townsend, P.A. (2017). The future of evapotranspiration: Global requirements for ecosystem functioning, carbon and climate feedbacks, agricultural management, and water resources. *Water Resources Research*, 53, 2618-2626
- Fisher, J.B., Tu, K.P., & Baldocchi, D.D. (2008). Global estimates of the land-atmosphere water flux based on monthly AVHRR and ISLSCP-II data, validated at 16 FLUXNET sites. *Remote Sensing of Environment*, 112, 901-919
- Fisher, J.B., Whittaker, R.J., & Malhi, Y. (2011). ET come home: potential evapotranspiration in geographical ecology. *Global Ecology and Biogeography*, 20, 1-18
- González-Dugo, M.P., Chen, X., Andreu, A., Carpintero, E., Gómez-Giraldez, P.J., Carrara, A., & Su, Z. (2021). Long-term water stress and drought assessment of Mediterranean oak savanna vegetation using thermal remote sensing. *Hydrology and Earth System Sciences*, 25, 755-768

- Gupta, H.V., Kling, H., Yilmaz, K.K., & Martinez, G.F. (2009). Decomposition of the mean squared error and NSE performance criteria: Implications for improving hydrological modelling. *Journal of Hydrology*, 377, 80-91
- Guzinski, R., Anderson, M.C., Kustas, W.P., Nieto, H., & Sandholt, I. (2013). Using a thermal-based two source energy balance model with time-differencing to estimate surface energy fluxes with day–night MODIS observations. *Hydrology and Earth System Sciences*, 17, 2809-2825
- Hook, S.J., Cawse-Nicholson, K., Barsi, J., Radocinski, R., Hulley, G.C., Johnson, W.R., Rivera, G., & Markham, B. (2019). In-flight validation of the ECOSTRESS, Landsats 7 and 8 thermal infrared spectral channels using the Lake Tahoe CA/NV and Salton Sea CA automated validation sites. *IEEE Transactions on Geoscience and Remote Sensing*, 58, 1294-1302
- Hu, T., Renzullo, L.J., Cao, B., van Dijk, A.I.J.M., Du, Y., Li, H., Cheng, J., Xu, Z., Zhou, J., & Liu, Q. (2019). Directional variation in surface emissivity inferred from the MYD21 product and its influence on estimated surface upwelling longwave radiation. *Remote Sensing of Environment*, 228, 45-60
- Hulley, G.C., Göttsche, F.M., Rivera, G., Hook, S.J., Freepartner, R.J., Martin, M.A., Cawse-Nicholson, K., & Johnson, W.R. (2021). Validation and quality assessment of the ECOSTRESS level-2 land surface temperature and emissivity product. *IEEE Transactions on Geoscience and Remote Sensing*, 60, 1-23
- Jaafar, H., Mourad, R., & Schull, M. (2022). A global 30-m ET model (HSEB) using harmonized Landsat and Sentinel-2, MODIS and VIIRS: Comparison to ECOSTRESS ET and LST. *Remote Sensing of Environment*, 274, 112995
- Jasechko, S., Sharp, Z.D., Gibson, J.J., Birks, S.J., Yi, Y., & Fawcett, P.J. (2013). Terrestrial water fluxes dominated by transpiration. *Nature*, 496, 347-350
- Koetz, B., Bastiaanssen, W., Berger, M., Defournay, P., Del Bello, U., Drusch, M., Drinkwater, M., Duca, R., Fernandez, V., & Ghent, D. (2019). Agriculture: Land Surface Temperature Monitoring (LSTM) Mission. In: *2019 ESA Living Planet Symposium*. Milan, Italy
- Kustas, W., & Anderson, M. (2009). Advances in thermal infrared remote sensing for land surface modeling. *Agricultural and Forest Meteorology*, 149, 2071-2081
- Kustas, W.P., Nieto, H., Morillas, L., Anderson, M.C., Alfieri, J.G., Hipps, L.E., Villagarcía, L., Domingo, F., & Garcia, M. (2016). Revisiting the paper “Using radiometric surface temperature for surface energy flux estimation in Mediterranean drylands from a two-source perspective”. *Remote Sensing of Environment*, 184, 645-653
- Lagouarde, J.P., Bhattacharya, B.K., Crebassol, P., Gamet, P., Babu, S.S., Boulet, G., Briottet, X., Buddhiraju, K.M., Cherchali, S., & Dadou, I. (2018). The Indian-French Trishna mission: Earth observation in the thermal infrared with high spatio-temporal resolution. In: *2018 IEEE International Geoscience and Remote Sensing Symposium* (pp. 4078-4081). Valencia, Spain
- Li, Y., Kustas, W.P., Huang, C., Nieto, H., Haghighi, E., Anderson, M.C., Domingo, F., Garcia, M., & Scott, R.L. (2019). Evaluating soil resistance formulations in thermal-based two-source energy balance (TSEB) model: Implications for heterogeneous semiarid and arid regions. *Water Resources Research*, 55, 1059-1078
- Liu, N., Oishi, A.C., Miniati, C.F., & Bolstad, P. (2021). An evaluation of ECOSTRESS products of a temperate montane humid forest in a complex terrain environment. *Remote Sensing of Environment*, 265, 112662
- Mallick, K., Baldocchi, D., Jarvis, A., Hu, T., Trebs, I., Sulis, M., Bhattarai, N., Bossung, C., Eid, Y., & Cleverly, J. (2022). Insights into the Aerodynamic versus Radiometric Surface Temperature

- Debate in Thermal-based Evaporation Modeling. *Geophysical Research Letters*, 49, e2021GL097568
- Mallick, K., Boegh, E., Trebs, I., Alfieri, J.G., Kustas, W.P., Prueger, J.H., Niyogi, D., Das, N., Drewry, D.T., & Hoffmann, L. (2015). Reintroducing radiometric surface temperature into the Penman-Monteith formulation. *Water Resources Research*, 51, 6214-6243
- Mallick, K., Hu, T., Bai, Y., Bhattarai, N., Trebs, I., Schlerf, M., Boulet, G., Wang, T., Sanchez, C.R., & Shortt, R. (2021). Thermal and Shortwave Infrared Remote Sensing of Ecosystem Processes: Opportunities, Synergies, and Challenges. In: *2021 IEEE International India Geoscience and Remote Sensing Symposium (InGARSS)* (pp. 440-443). Ahmedabad, India
- Mallick, K., Jarvis, A.J., Boegh, E., Fisher, J.B., Drewry, D.T., Tu, K.P., Hook, S.J., Hulley, G., Ardö, J., & Beringer, J. (2014). A Surface Temperature Initiated Closure (STIC) for surface energy balance fluxes. *Remote Sensing of Environment*, 141, 243-261
- Mallick, K., Toivonen, E., Trebs, I., Boegh, E., Cleverly, J., Eamus, D., Koivusalo, H., Drewry, D., Arndt, S.K., & Griebel, A. (2018a). Bridging Thermal Infrared Sensing and Physically-Based Evapotranspiration Modeling: From Theoretical Implementation to Validation Across an Aridity Gradient in Australian Ecosystems. *Water Resources Research*, 54, 3409-3435
- Mallick, K., Trebs, I., Boegh, E., Giustarini, L., Schlerf, M., Drewry, D.T., Hoffmann, L., Von Randow, C., Kruijt, B., & Araùjo, A. (2016). Canopy-scale biophysical controls of transpiration and evaporation in the Amazon Basin. *Hydrology and Earth System Sciences*, 20, 4237-4264
- Mallick, K., Wandera, L., Bhattarai, N., Hostache, R., Kleniewska, M., & Chormanski, J. (2018b). A critical evaluation on the role of aerodynamic and canopy-surface conductance parameterization in SEB and SVAT models for simulating evapotranspiration: A case study in the upper biebrza national park wetland in poland. *Water*, 10, 1753
- Mao, J., Fu, W., Shi, X., Ricciuto, D.M., Fisher, J.B., Dickinson, R.E., Wei, Y., Shem, W., Piao, S., & Wang, K. (2015). Disentangling climatic and anthropogenic controls on global terrestrial evapotranspiration trends. *Environmental Research Letters*, 10, 094008
- Massman, W.J. (1997). An analytical one-dimensional model of momentum transfer by vegetation of arbitrary structure. *Boundary-Layer Meteorology*, 83, 407-421
- Mwangi, S., Boulet, G., & Olioso, A. (2022). Assessment of an extended SPARSE model for estimating evapotranspiration from directional thermal infrared data. *Agricultural and Forest Meteorology*, 317, 108882
- Nieto, H., Guzinski, R., Kustas, W.P., & Andreu, A. (2016). pyTSEB. <https://github.com/hectornieto/pyTSEB>
- Norman, J.M., Kustas, W.P., & Humes, K.S. (1995). Source approach for estimating soil and vegetation energy fluxes in observations of directional radiometric surface temperature. *Agricultural and Forest Meteorology*, 77, 263-293
- Otkin, J.A., Anderson, M.C., Hain, C., Mladenova, I.E., Basara, J.B., & Svoboda, M. (2013). Examining rapid onset drought development using the thermal infrared-based evaporative stress index. *Journal of Hydrometeorology*, 14, 1057-1074
- Ryu, Y., Baldocchi, D.D., Kobayashi, H., Van Ingen, C., Li, J., Black, T.A., Beringer, J., Van Gorsel, E., Knohl, A., & Law, B.E. (2011). Integration of MODIS land and atmosphere products with a coupled-process model to estimate gross primary productivity and evapotranspiration from 1 km to global scales. *Global Biogeochemical Cycles*, 25, GB4017
- Senay, G.B., Bohms, S., Singh, R.K., Gowda, P.H., Velpuri, N.M., Alemu, H., & Verdin, J.P. (2013). Operational evapotranspiration mapping using remote sensing and weather datasets: A

- new parameterization for the SSEB approach. *JAWRA Journal of the American Water Resources Association*, 49, 577-591
- Shuttleworth, W.J., & Wallace, J.S. (1985). Evaporation from sparse crops-an energy combination theory. *Quarterly Journal of the Royal Meteorological Society*, 111, 839-855
- Su, Z. (2002). The Surface Energy Balance System (SEBS) for estimation of turbulent heat fluxes. *Hydrology and Earth System Sciences*, 6, 85-100
- Trebs, I., Mallick, K., Bhattarai, N., Sulis, M., Cleverly, J., Woodgate, W., Silberstein, R., Hinko-Najera, N., Beringer, J., & Meyer, W.S. (2021). The role of aerodynamic resistance in thermal remote sensing-based evapotranspiration models. *Remote Sensing of Environment*, 264, 112602
- Xiao, J., Fisher, J.B., Hashimoto, H., Ichii, K., & Parazoo, N.C. (2021). Emerging satellite observations for diurnal cycling of ecosystem processes. *Nature Plants*, 7, 877-887
- Yang, Y., Long, D., Guan, H., Liang, W., Simmons, C., & Batelaan, O. (2015). Comparison of three dual-source remote sensing evapotranspiration models during the MUSOEXE-12 campaign: Revisit of model physics. *Water Resources Research*, 51, 3145-3165
- Zomer, R.J., & Trabucco, A. (2022). Version 3 of the “Global Aridity Index and Potential Evapotranspiration (ET0) Database”. <https://doi.org/10.6084/m9.figshare.7504448.v4>